Numerical conformal mapping and mesh generation for polygonal and multiply-connected regions

B. Lin and S. N. Chandler-Wilde

ABSTRACT

Details are given of a boundary-fitted mesh generation method for use in modelling free surface flow and water quality. A numerical method has been developed for generating conformal meshes for curvilinear polygonal and multiply-connected regions. The method is based on the Cauchy-Riemann conditions for the analytic function and is able to map a curvilinear polygonal region directly onto a regular polygonal region, with horizontal and vertical sides. A set of equations have been derived for determining the lengths of these sides and the least-squares method has been used in solving the equations. Several numerical examples are presented to illustrate the method.

Key words | analytic function, boundary integral equations, conformal mapping, mesh generation, multiply-connected region, numerical methods

B. Lin (corresponding author)
School of Engineering,
Cardiff University,
Cardiff CF2 3TB,
UK

S. N. Chandler-Wilde
Department of Mathematics and Statistics,
Brunel University,
Uxbridge,
Middlesex UB8 3PH,
UK

1. INTRODUCTION

Numerical mesh generation has now become a common tool in computational fluid dynamics. In recent years, numerical conformal mapping methods have been increasingly used for mesh generation. The main advantages of using conformal mapping are: (a) it has a very strong theoretical background in complex function theory and so many of the results of analytical function theory are useful in the mesh generation process; and (b) the original governing partial differential equations acquire a minimum number of extra terms on transformation, so that the solution methods developed for Cartesian co-ordinates may still be applicable with only minor changes. For some hydrodynamic modelling problems, e.g. the parabolic approximations for water waves, it has been found that the most suitable boundary-fitted grids are those based on conformal co-ordinate systems (Kirby *et al*. 1994).

Among conformal mapping methods, perhaps the most applicable for mapping arbitrarily shaped polygons is the Schwarz-Christoffel transformation. This method maps the upper half of one complex plane onto the interior of a polygon. In the case of curvilinear regions, Schwarz-Christoffel based methods have mostly been accomplished by approximating the curved edges by many straight line segments, or other easily defined arcs (Elcrat & Trefethen 1986). However, determination of the parameters for this transformation is very difficult and requires considerable computational effort, since numerical integration of complex functions involving singularities is often encountered (Chaudhry & Schinzinger 1992*a*, *b*). Rapid progress has been made in directly mapping a quadrilateral onto a rectangle using the methods of numerical conformal mapping (Papamicheal 1989).

The main objective of this paper is to develop a boundary-fitted curvilinear system for modelling free surface flow and water quality. The method of mapping a simply connected region (Chandler-Wilde & Lin 1992; Lin & Chandler-Wilde 1996) has been extended to a more general geometry, i.e. multiply-connected region. An algorithm has been developed for numerically mapping a general curvilinear polygonal region with $2n$ curved sides onto a polygon with $2n$ straight sides. When applied to mesh generation for hydrodynamic and environmental modelling, the method makes the specification of boundary conditions easier, since the computational domain is 'similar' to the physical domain in the sense that the sides are in one-to-one correspondence.

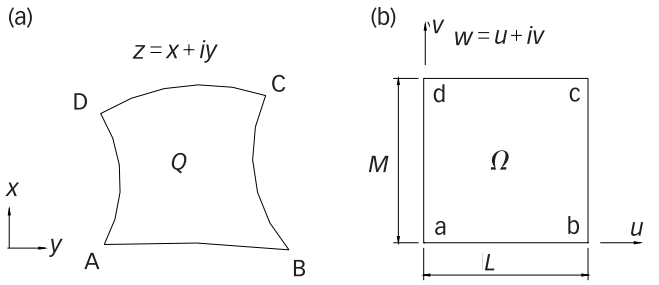

Figure 1 | Mapping a quadrilateral onto a rectangle. (a) General quadrilateral; (b) rectangle.

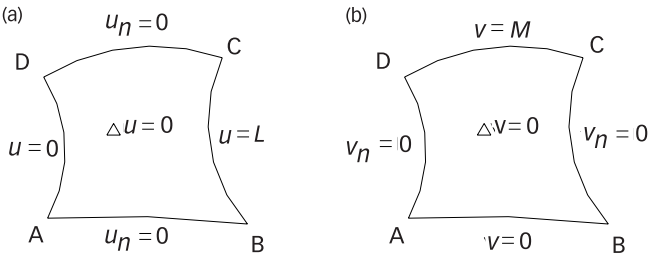

Figure 2 | Laplace equations and boundary conditions for u and v. (a) For u=Re(F); (b) For v=Im(F).

In section 2, details of the algorithm for mapping onto the multiply-connected polygon are given. Section 3 discusses the inverse mapping and section 4 presents several examples.

2. MAPPING ONTO MULTIPLY-CONNECTED POLYGONAL REGIONS

From complex function theory (Henrici 1986) we know that the quadrilateral {Q: A, B, C, D} shown in Figure 1a is conformally equivalent to the rectangle {Ω: a, b, c, d} shown in Figure 1b, if the ratio L/M is equal to m, the conformal module of {Q: A, B, C, D}. If $F = u + iv$ is the mapping function F: $Q \rightarrow \Omega$, then u and v satisfy the Laplace equations

$$\frac{\partial^2 u}{\partial x^2} + \frac{\partial^2 u}{\partial y^2} = 0 \qquad \text{and} \quad \frac{\partial^2 v}{\partial x^2} + \frac{\partial^2 v}{\partial y^2} = 0, \tag{1}$$

inside Q, and the Cauchy-Riemann equations

$$\frac{\partial u}{\partial s} = \frac{\partial v}{\partial n}, \qquad \frac{\partial u}{\partial n} = -\frac{\partial v}{\partial s}, \tag{2}$$

at the boundaries, where ∂s and ∂n denote the tangential and normal derivatives respectively, s-directed counterclockwise around Q, and n directed into Q (see Figure 2a, b).

Based on this theory, a numerical method for mapping polygonal regions has been developed (Lin & Chandler-Wilde 1996). By this method a general polygonal region with curved edges can be mapped onto a regular polygonal region with the same number of horizontal and vertical edges. In the following details are given of the extension of the conformal method to multiply-connected regions.

Consider the general K-connected region Q in Figure 3a and the corresponding rectilinear K-connected region Ω in Figure 3b. The boundary of Ω consists of K disjoint closed rectilinear Jordan curves. The kth polygon has $N(k)$ sides ($N(k)$ even). For $m = 2, 4, \ldots, N(k)$, the mth side is a horizontal line, $u = U(k)_m$, and

$$\begin{cases} V(k)_{m-1} \le v \le V(k)_{m+1} & \text{for} \quad V(k)_{m+1} > V(k)_{m-1} \\ V(k)_{m-1} \ge v \ge V(k)_{m+1} & \text{for} \quad V(k)_{m+1} < V(k)_{m-1} \end{cases},$$

and for $m = 1, 3, \ldots, N(k)$-1, the mth side is a vertical line, $v = V(k)m$, and

$$\begin{cases} U(k)_{m-1} \le u \le U(k)_{m+1} & \text{for} \quad U(k)_{m+1} > U(k)_{m-1} \\ U(k)_{m-1} \ge u \ge U_{m+1} & \text{for} \quad U(k)_{m+1} < U(k)_{m-1} \end{cases}.$$

Assume there is a conformal mapping F: $Q \rightarrow \Omega$, in which $F = u + iv$, which conformally maps Q onto Ω. Then u and v satisfy the Laplace equations (1) in Q and the Cauchy-Riemann equations (2) at the boundaries, giving rise to the boundary value problems shown in Figure 4.

Let $U(k)^{(2i)}$ be the solution of the boundary value problem in Figure 4a when $U(j)_{2m} = \delta_{im}\delta_{jk}$, in which $\delta_{im} = 1$ when $i = m$, $\delta_{im} = 0$ when $i \neq m$, $j = 1, 2, \ldots, K$, $m = 1, 2, \ldots, N(k)/2$, and $V(k)^{(2i-1)}$ be the solution of the boundary value problem in Figure 4(b) when $V(j)_{2m-1} = \delta_{im}\delta_{jk}$,

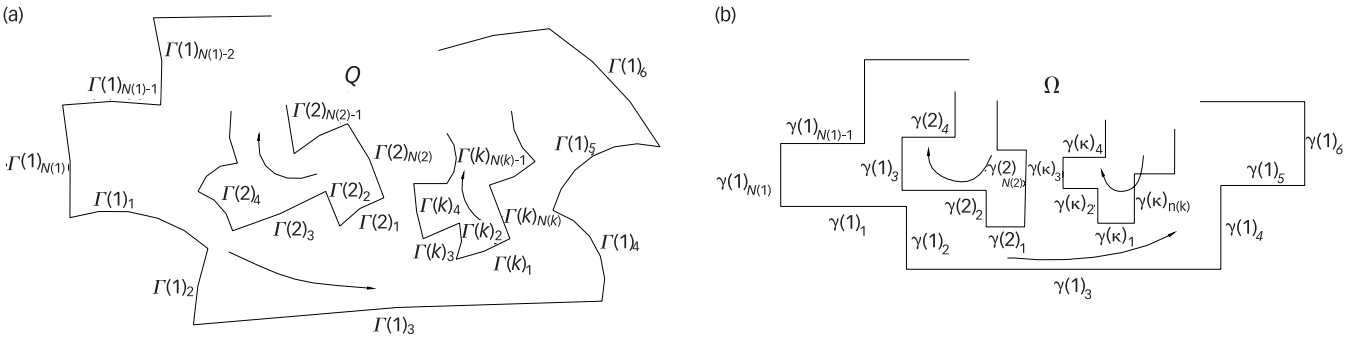

Figure 3 | Mapping a curvilinear multiply-connected region onto a rectilinear region. (a) Curvilinear polygonal region; (b) rectilinear region.

$j = 1, 2, \ldots, K$, $m = 1, 2, \ldots, N(k)/2$, for $i = 1, 2, \ldots, N(k)/2$, $k = 1, 2, \ldots, K$. Then

$$u = \sum_{k=1}^{K} \sum_{m=1}^{N(k)/2} U(k)_{2m} U(k)^{(2m)} \tag{3a}$$

$$v = \sum_{k=1}^{K} \sum_{m=1}^{N(k)/2} V(k)_{2m-1} V(k)^{(2m-1)} \tag{3b}$$

The boundary conditions in Figure 4 follow from the Cauchy-Riemann equations (2). Thus we have,

$$\int_{\Gamma(k)j} \frac{\partial u}{\partial n}\, \mathrm{d}s = V(k)_{j-1} - V(k)_{j+1}, \quad j = 2,4,\ldots,N(k), k = 1,2,\ldots,K \tag{4a}$$

and

$$\int_{\Gamma(k)j} \frac{\partial v}{\partial n}\, \mathrm{d}s = U(k)_{j+1} - U(k)_{j-1}, \quad j = 1,3,\ldots,N(k)\text{-}1, k = 1,2,\ldots,K. \tag{4b}$$

Note that s is directed counter-clockwise on the outer boundary, but clockwise on rest of the boundaries (see Figure 3) and we have defined

$$V(k)_{N(k)+1} = V(k)_1, \tag{5a}$$

$$U(k)_0 = U(k)_{N(k)}, \tag{5b}$$

for $k = 1, 2, \ldots, K$. Substituting from (4) into (5) we obtain,

$$\sum_{k=1}^{K} \sum_{m=1}^{N(k)/2} U(k)_{2m} \int_{\Gamma(k)j} \frac{\partial U(k)^{(2m)}}{\partial n}\, \mathrm{d}s = V(k)_{j-1} - V(k)_{j+1} \quad j = 2,4,\ldots,N(k), k = 1,2,\ldots,K, \tag{6a}$$

$$\sum_{k=1}^{K} \sum_{m=1}^{N(k)/2} V(k)_{2m-1} \int_{\Gamma(k)j} \frac{\partial V(k)^{(2m-1)}}{\partial n}\, \mathrm{d}s = U(k)_{j+1} - U(k)_{j-1} \quad j = 1,3,\ldots,N(k)\text{-}1, k = 1,2,\ldots,K. \tag{6b}$$

Equations (6) can be rewritten in matrix form,

$$\mathbf{MX} = \begin{bmatrix} \mathbf{A} & \mathbf{B} \\ \mathbf{C} & \mathbf{D} \end{bmatrix} \begin{bmatrix} \mathbf{V} \\ \mathbf{U} \end{bmatrix} = 0, \tag{7}$$

where

$$\mathbf{V} = \{V(1)_1, V(1)_3, \ldots, V(1)_{N(1)-1}, V(2)_1, V(2)_3, \ldots, V_{2N(2)-1}, \ldots, V(K)_1, V(K)_3, \ldots, V(K)_{N(K)-1}\}^T$$

$$\mathbf{U} = \{U(1)_2, U(1)_4, \ldots, U(1)_{N(1)}, U(2)_4, U(2)_4, \ldots, U_{2N(2)}, \ldots, U(K)_2, U(K)_4, \ldots, U(K)_{N(K)}\}^T,$$

$$\mathbf{A} = \begin{bmatrix} \mathbf{A}_1 & & & \\ & \mathbf{A}_2 & & \\ & & \cdots & \\ & & & \mathbf{A}_K \end{bmatrix}, \quad \mathbf{B} = \begin{bmatrix} \mathbf{B}_{11} & \mathbf{B}_{11} & \cdots & \mathbf{B}_{1K} \\ \mathbf{B}_{21} & \mathbf{B}_{22} & \cdots & \mathbf{B}_{2K} \\ & & \cdots & \\ \mathbf{B}_{K1} & \mathbf{B}_{2K} & \cdots & \mathbf{B}_{KK} \end{bmatrix},$$

$$\mathbf{C} = \begin{bmatrix} \mathbf{C}_{11} & \mathbf{C}_{11} & \cdots & \mathbf{C}_{1K} \\ \mathbf{C}_{21} & \mathbf{C}_{22} & \cdots & \mathbf{C}_{2K} \\ & & \cdots & \\ \mathbf{C}_{K1} & \mathbf{C}_{2K} & \cdots & \mathbf{C}_{KK} \end{bmatrix}, \quad \mathbf{D} = \begin{bmatrix} \mathbf{D}_1 & & & \\ & \mathbf{D}_2 & & \\ & & \cdots & \\ & & & \mathbf{D}_K \end{bmatrix},$$

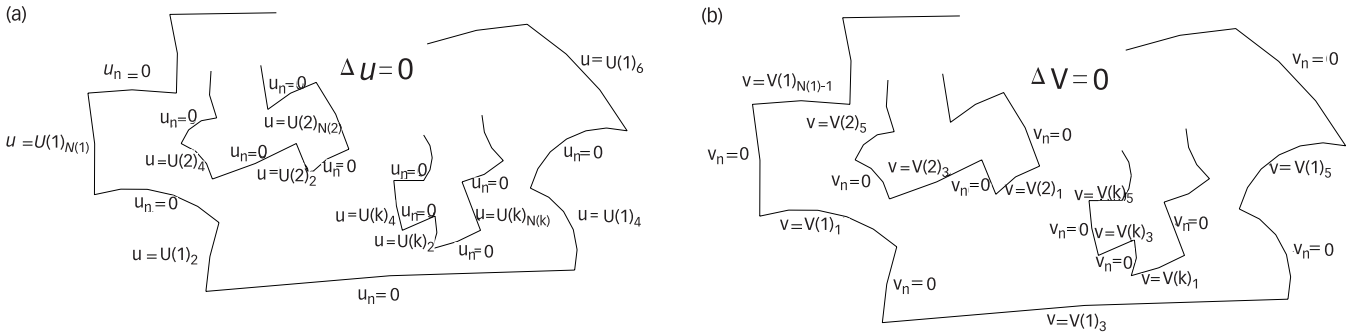

Figure 4 | Laplace equations and boundary conditions for u and v. For u=Re(F);(b) for v=Im(F).

with

$$\mathbf{A}_k=\begin{bmatrix} -1 & 1 & & \\ & \cdots & & \\ & & -1 & 1 \\ 1 & & & -1 \end{bmatrix}_{N(k)/2\times N(k)/2},$$

$$\mathbf{B}_{ij}=\begin{bmatrix} b_2^2 & b_2^4 & \cdots & b_2^{N(j)} \\ b_4^2 & b_4^4 & \cdots & b_4^{N(j)} \\ & & \cdots & \\ b_{N(i)}^2 & b_{N(i)}^4 & \cdots & b_{N(i)}^{N(j)} \end{bmatrix}_{N(i)/2\times N(j)/2},$$

$$\mathbf{C}_{ij}=\begin{bmatrix} c_1^1 & c_1^3 & \cdots & c_1^{N(j)-1} \\ c_3^1 & c_3^3 & \cdots & c_3^{N(j)-1} \\ & & \cdots & \\ c_{N(i)-1}^1 & c_{N(i)-1}^3 & \cdots & c_{N(i)-1}^{N(j)-1} \end{bmatrix}_{N(i)/2\times N(j)/2},$$

$$\mathbf{D}_k=\begin{bmatrix} -1 & & & 1 \\ 1 & -1 & & \\ & & \cdots & \\ & & 1 & -1 \end{bmatrix}_{N(k)/2\times N(k)/2},$$

and

$$b_n^m=\int_{\Gamma(i)_n}\frac{\partial U(j)^{(m)}}{\partial n}\,\mathrm{d}s,$$

$$c_n^m=\int_{\Gamma(i)_n}\frac{\partial V(j)^{(m)}}{\partial n}\,\mathrm{d}s.$$

Note that one of equations (6a) and one of equations (6b) are redundant from the condition,

$$\oint_{\partial Q}\frac{\partial u}{\partial n}\,\mathrm{d}s=\oint_{\partial Q}\frac{\partial v}{\partial n}\,\mathrm{d}s=0. \tag{8}$$

Equation (7) is solved by the least-squares method. To ensure a definite position in the computational plan, we set $U(1)_{N(1)}=V(1)_1=0$, and $V(1)^{2m-1}$ to unity.

To compute the map F on the boundary, the following scheme is employed:

(1) Use the boundary integral method (Kress 1989) to solve the boundary value problems for $U(k)^{(2m)}$ and $V(k)^{(2m-1)}$ for $m=1, 2, \ldots, N(k)/2$, and obtain $U(k)^{(2m)}$ and $V(k)^{(2m-1)}$ and $\partial U(k)^{(2m)}/\partial n$ and $\partial V(k)^{(2m-1)}/\partial n$ on the boundary.
(2) Solve equation (7) together with the condition $V(1)^{2m-1}=1$, using the least-squares method (Gill *et al.* 1991), and approximating the integrals in the matrix **M** by the midpoint rule.
(3) Compute $F=u+iv$ on the boundary using formulas (3).

3. INVERSE MAP

By Cauchy's integral formula (Brebbia & Dominguez 1989) we have, for every point $P\in\Omega$,

$$g(P)=\frac{1}{2\pi i}\oint_{\partial\Omega}\frac{g(w)}{w-P}\,\mathrm{d}w. \tag{9}$$

Let y be a typical straight side of (see Figure 3a, b). We have already determined $g(w)$ at points $w_i = F(z_i)$, $i = 0, 1, 2, \ldots, N$, where N is the number of boundary elements on Γ and $z_0, z_1, \ldots z_N$ are the end points of boundary elements on the image of y.

Let

$$g_i = g(w_i), \quad i = 0, 1, 2, \ldots, N \tag{10}$$

$$I(P) = \frac{1}{2\pi i} \int_y \frac{g(w)}{w-P}\, dw\,. \tag{11}$$

Then

$$I(P) = \frac{1}{2\pi i} \sum_{i=1}^{N} \int_{w_{i-1}}^{w_i} \frac{g(w)}{w-P}\, dw$$

$$\approx I_N(P) = \frac{1}{2\pi i} \sum_{i=1}^{N} \frac{1}{w_i - w_{i-1}} \int_{w_{i-1}}^{w_i} \frac{g_{i-1}(w_i - w) + g_i(w - w_{i-1})}{w-P}\, dw \tag{12}$$

where $g(w)$ has been approximated by linear interpolation on the interval (w_{i-1}, w_i). Equation (12) can be rewritten as,

$$I_{NJ}(P) = \frac{1}{2\pi i} \sum_{i=0}^{NJ} g_i w_i(P)\,, \tag{13}$$

where,

$$w_0(P) = \frac{1}{w_1 - w_0} \int_{w_0}^{w_1} \frac{w_1 - w}{w-p}\, dw = -1 + \frac{P - w_1}{w_1 - w_0} \ln\left(\frac{w_0 - P}{w_1 - P}\right)$$

$$w_i(P) = \frac{1}{w_{i+1} - w_i} \int_{w_i}^{w_{i+1}} \frac{w_{i+1} - w}{w-p}\, dw + \frac{1}{w_i - w_{i-1}} \int_{w_{i-1}}^{w_i} \frac{w - w_{i-1}}{w-p}\, dw$$

$$= \frac{P - w_{i-1}}{w_i - w_{i-1}} \ln\left(\frac{w_i - P}{w_{i-1} - P}\right) - \frac{P - w_{i+1}}{w_{i+1} - w_{i-1}} \ln\left(\frac{w_{i+1} - P}{w_i - P}\right)$$

$i = 1, 2, \ldots, N\text{-}1$

$$w_N(P) = \frac{1}{w_N - w_{N-1}} \int_{w_{N-1}}^{w_N} \frac{w - w_{N-1}}{w-p}\, dw$$

$$= 1 + \frac{P - w_{NJ-1}}{w_{NJ} - w_{NJ-1}} \ln\left(\frac{w_{NJ} - P}{w_{NJ-1} - P}\right)\,.$$

Note that, for $|P - w_i| \gg h = |w_i - w_{i-1}|$,

$$\int_{w_{i-1}}^{w_i} \frac{w - w_i}{w-p}\, dw \approx \int_{w_{i-1}}^{w_i} \frac{w - w_i}{w_i - p}\, dw = \frac{1}{2} \frac{h^2}{w_i - P}\,.$$

In our computations, $w_i(P)$ is approximated by

$$w_i(P) \approx \begin{cases} \dfrac{h}{w_i - P} & i = 1,2, \ldots, NJ-1 \\ \dfrac{1}{2} \dfrac{h}{w_i - P} & i = 0, NJ \end{cases} \tag{14}$$

when

$$\left| \frac{P - w_{i-1}}{w_i - w_{i-1}} \right| \geq 20\,.$$

4. APPLICATIONS

Example 1

Consider a rectangle Ω in the w-plane,

$$\Omega = \{(u,v);\ 1 \leq u \leq 3,\ 1 \leq v \leq 2\}$$

and

$$a = 1 + i,\ \ b = 3 + i,\ \ c = 3 + 2i,\ \ d = 1 + 2i,$$

as shown in Figure 5a. The quadrilateral Q\{A, B, C, D\} is defined by the mapping Ω using the function $z = G(w) = w \times w$ with

$$A = a \times a,\ \ B = b \times b,\ \ C = c \times c,\ \ D = d \times d.$$

Now we are going to determine the conformal module $m(Q)$ and then re-map Q onto Ω. It is clear that the conformal module $m = ab = 2$. Table 1 lists the predicted module m, its error for different number of

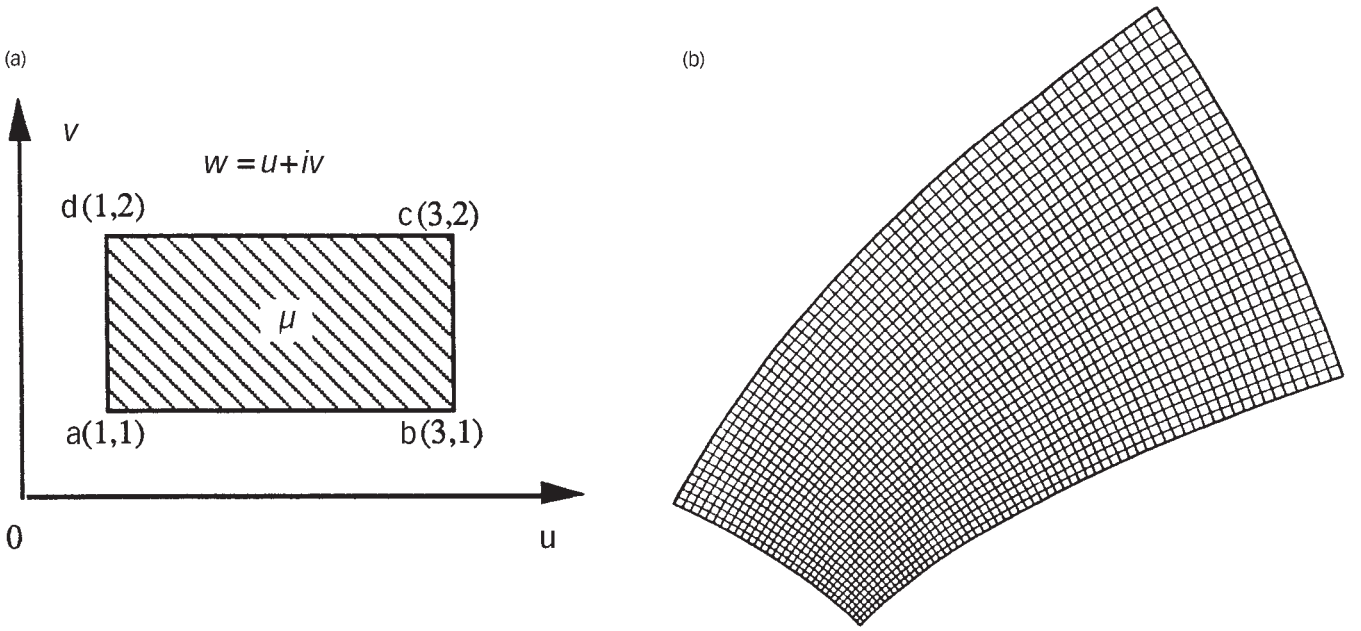

Figure 5 | Mapping a quadrilateral.

elements and the convergence rate R, which is defined as:

$$R = \log_2(E_{ne\times 2}/E_{ne}) \tag{15}$$

where the footnote *ne* stands for the number of elements used, E for error.

It can be seen that the rate of convergence for m is about 1.6. The conformal module m is indeed converged to 2. Figure 5b shows the numerical mesh generated. On a Pentium 200 MHz computer, the CPU time required to generate the mesh is less than 2 minutes.

Table 1 | The convergence rate of module m

No. of elements	M_{ne}	E_{ne}	R
12	2.05495	0.05495	
24	2.01920	0.01920	1.52
48	2.00628	0.00628	1.60
96	2.00202	0.00202	1.63
192	2.00065	0.00065	1.63
384	2.00021	0.00021	1.63

Example 2

Consider a polygon domain Ω in the w-plane, with 12 straight boundary segments, as illustrated in Figure 6a. If we define a conformal mapping

$$z = 0.5e^{0.5w} + 0.5w^2$$

then the mapped region Q in the z-plane is shown in Figure 6b. The purpose of this example is to test whether the above mentioned method is able to map the domain Q in the z-plane back to the domain Ω in the w-plane. Thus if we set $V_3 = 1$, then the solution should be

$$\mathbf{U} = \{1.0 \quad 0.9 \quad 0.7 \quad 0.5 \quad 0.3 \quad 0.0\}^T$$

$$\mathbf{V} = \{0.6 \quad 1.0 \quad 0.4 \quad 0.8 \quad 0.2 \quad 0.0\}^T$$

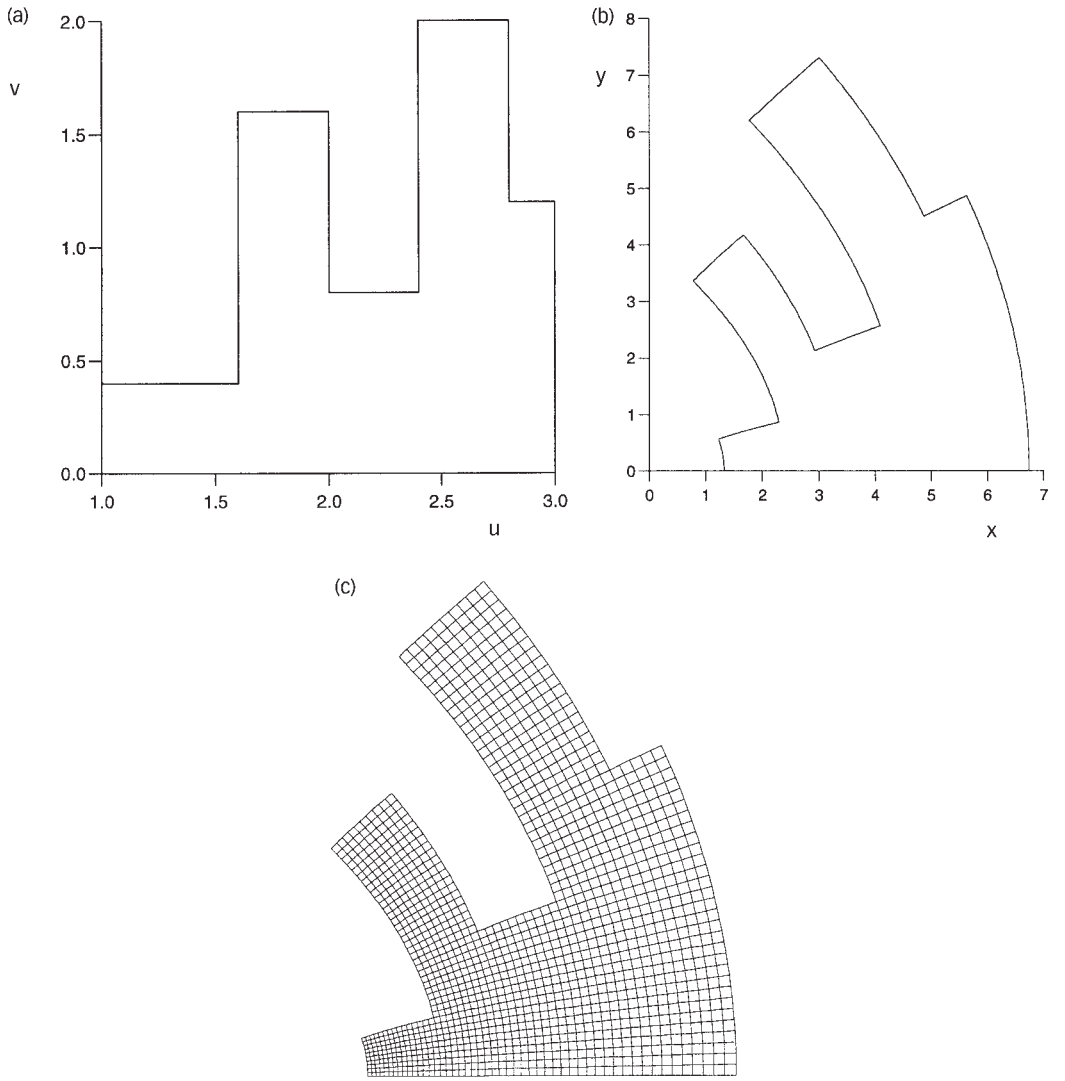

Figure 6 | Conformal mapping and mesh generation for a 12 sided curvilinear polygonal region.

Comparisons between the model predicted U_{2m} and V_{2m-1} and the analytical solutions are listed in Table 2a, b respectively.

As seen in the previous example, as the number of boundary elements increases the differences between the numerical results and the analytical solutions decrease. The inverse mapping is then carried out using 768 boundary elements. Figure 6c shows the conformal mesh model generated for the domain.

Example 3

The third example is to generate a conformal mesh for a practical application. Figure 7a shows the boundary of the Bristol Channel, UK. The physical domain is considered as a curvilinear polygonal region of six sides and it was mapped onto an L-shaped region, as shown in Figure 7b. The corner points ABCDEF in Figure 7a are mapped to abcdef in Figure 7b and the numerically generated conformal mesh is shown in Figure 7c.

Table 2a | Comparisons of computed results with the analytical solution

Ne	U_4	U_6	U_8	U_{10}	U_{12}	**max. error**
48	1.03800	0.92127	0.73177	0.54439	0.31771	
Error	0.03800	0.02127	0.03177	0.04439	0.01771	0.04439
96	1.01437	0.90813	0.71181	0.52036	0.30751	
Error	0.01437	0.00813	0.01181	0.02036	0.00751	0.02036
192	1.00543	0.90261	0.70403	0.50918	0.30294	
Error	0.00543	0.00261	0.00403	0.00918	0.00294	0.00918
384	1.00214	0.90082	0.70140	0.50428	0.30117	
Error	0.00214	0.00082	0.00140	0.00428	0.00117	0.00428
768	1.00094	0.90024	0.70051	0.50200	0.30043	
Error	0.00094	0.00024	0.00051	0.00200	0.00043	0.00200

Table 2b |

Ne	V_3	V_5	V_7	V_9	V_{11}	**max. error**
Error	0.00000	0.00041	0.07755	0.00451	0.01947	0.07755
96	1.00000	0.39871	0.83586	0.20231	0.60677	
Error	0.00000	0.00129	0.03586	0.00231	0.00677	0.03586
192	1.00000	0.39897	0.81683	0.20099	0.60288	
Error	0.00000	0.00103	0.01683	0.00099	0.00288	0.01683
384	1.00000	0.39938	0.80818	0.20043	0.60130	
Error	0.00000	0.00062	0.00818	0.00043	0.00130	0.00818
768	1.00000	0.39972	0.8041	0.20018	0.60073	
Error	0.00000	0.00028	0.00410	0.00018	0.00073	0.00410

It can be seen from Figure 7c that large grid cells still appear in regions of concave curvature and small grid cells appear in the vicinity of convex boundary curvature. This is a disadvantage of the conformal mapping, although this phenomenon can also be observed in most of the grids generated by elliptic methods without using control functions. One way to overcome the difficulty is to re-distribute the mesh using one-dimensional stretching

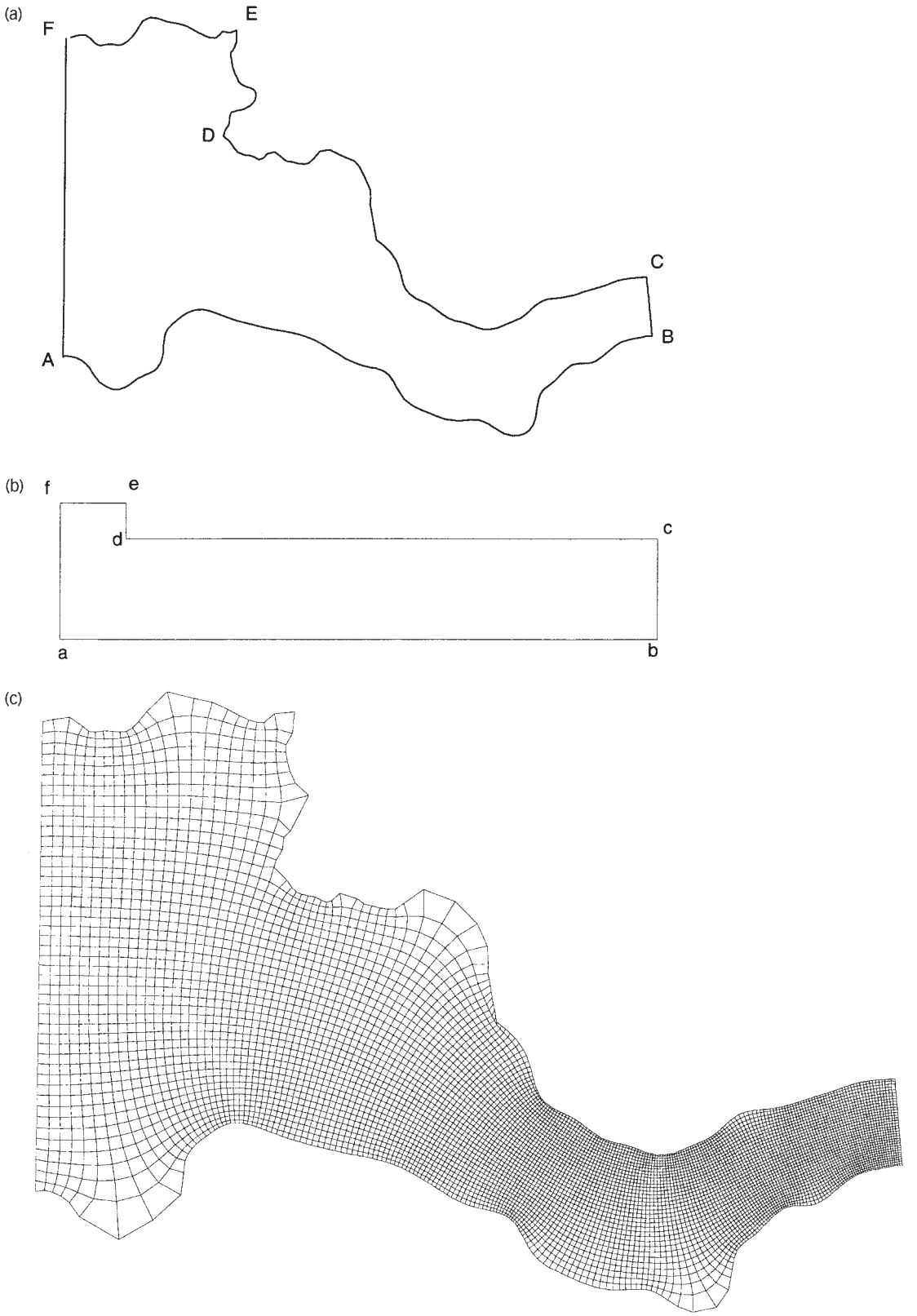

Figure 7 | Conformal mapping and mesh generation for Bristol Channel.

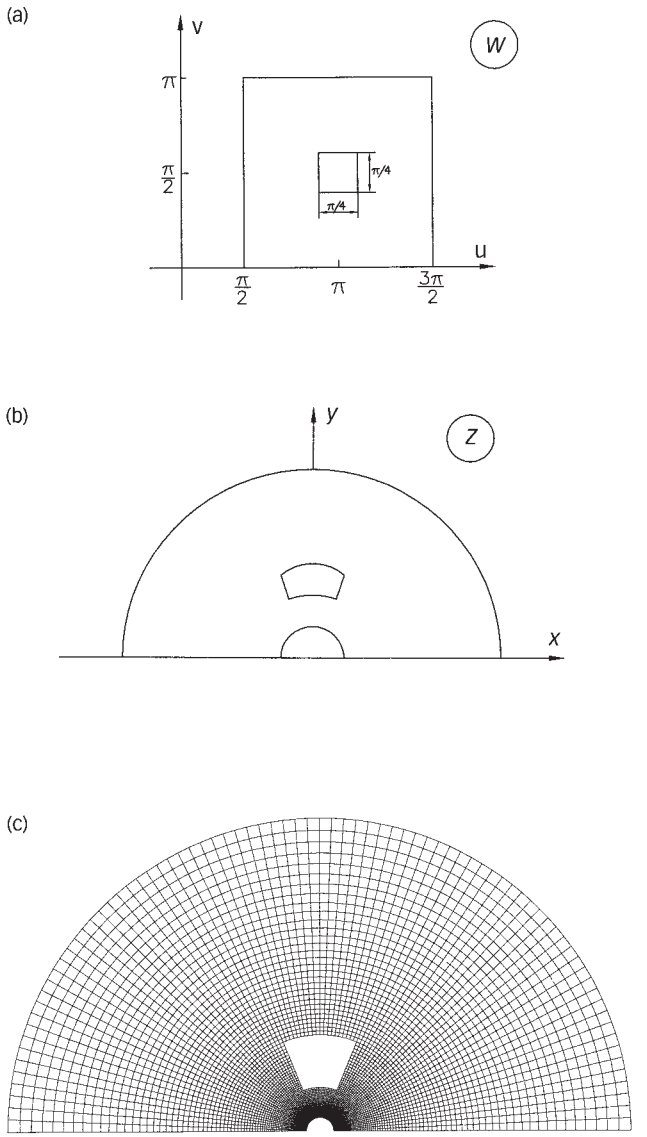

Figure 8 | Conformal mapping and mesh generation for a doubly connected region.

functions. The mesh thus generated remains orthogonal but no longer conformal (Lin & Chandler-Wilde 1996).

Example 4

Consider two doubly-connected domain Ω and Q as illustrated in Figure 8a, b, in which Q is generated by mapping Ω using the following transformation:

$$z = g(w) = e^{w}.$$

If we set $x_2 = 1$, then the solution $\mathbf{X}$ will be

$$\mathbf{X} = \{x_i\} = \{0.0 \quad 1.0 \quad 0.375 \quad 0.625 \quad 1.0 \quad 0.0 \quad 0.375 \quad 0.625\}^T.$$

Table 3 shows the comparisons between the computed and the analytical solutions, for x_3, x_4, x_5, x_7, x_8. It can be seen that the differences between the model predictions and the analytical results decrease as the number of boundary elements increases. Figure 8c gives the generated mesh on the physical domain. In this example, 480 boundary elements were used for the forward mapping, and 81×81 regular grids were used for the backward mapping.

Example 5

Figure 9a is also a doubly connected region. We first divide the circle into four arcs, P_1P_2, P_2P_3, P_3P_4 and P_4P_1, with each arc being submented by $\pi/2$, and then map the domain Q onto a regular domain as shown in

Table 3 | Comparisons of numerical results and analytical solution

ne	x_3	error	x_4	error	x_5	error	x_7	error	x_8	error	Max er.
60	0.37184	0.00384	0.62691	0.00191	0.99971	0.00029	0.37556	0.00056	0.62658	0.00158	0.00384
120	0.37247	0.00153	0.62591	0.00091	0.99980	0.00020	0.37502	0.00002	0.62523	0.00023	0.00153
240	0.37436	0.00064	0.62544	0.00044	0.99984	0.00016	0.37499	0.00001	0.62492	0.00008	0.00064
480	0.37470	0.00030	0.62533	0.00023	0.99987	0.00013	0.37501	0.00001	0.62486	0.00014	0.00030

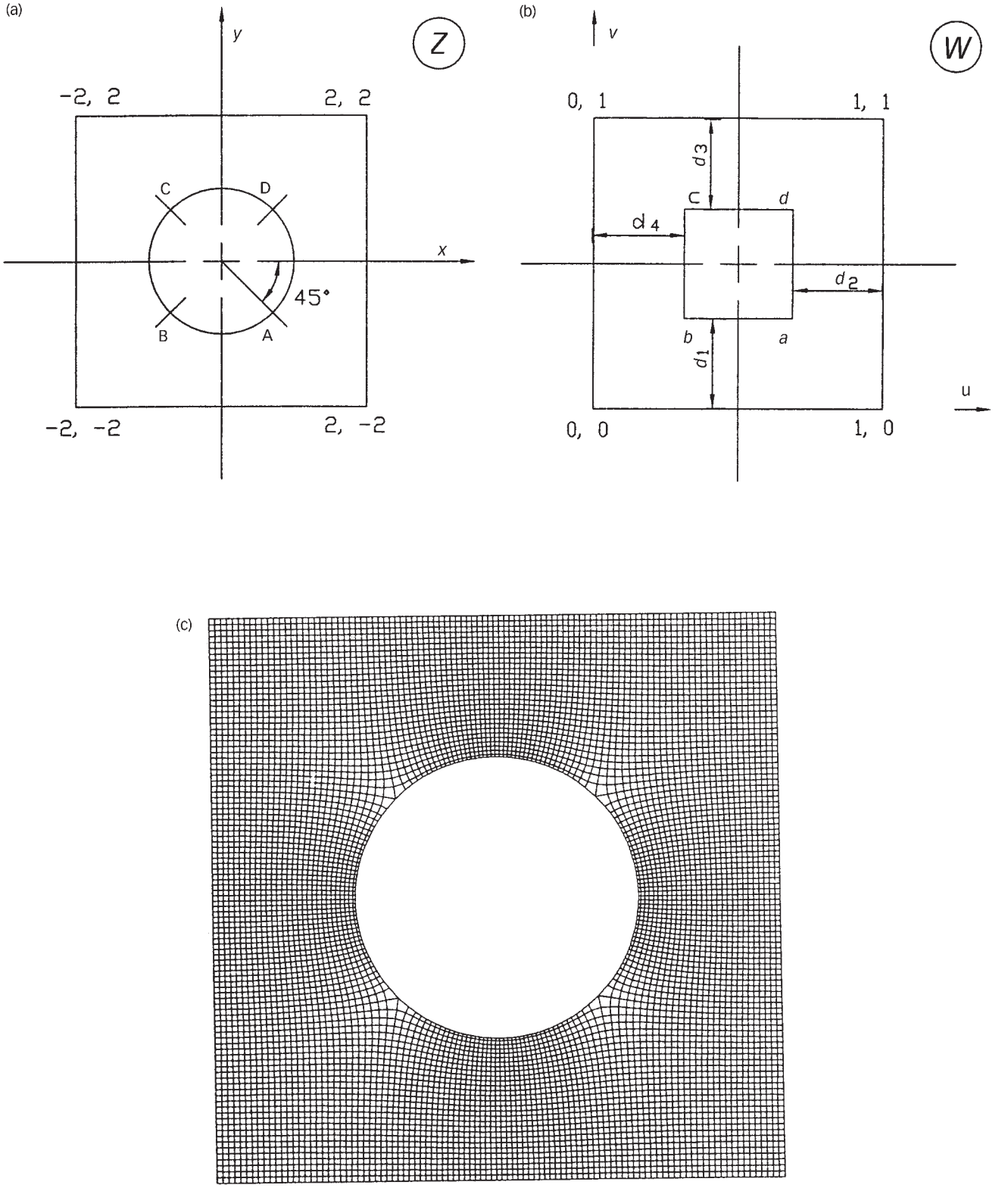

Figure 9 | Conformal mapping and mesh generation for a doubly connected region.

Table 4 | Convergence test for a doubly connected region

ne	d_{av}	d_1–d_{av}	d_2–d_{av}	d_{13}–d_{av}	d_4–d_{av}	**max**
60	0.28734	0.00050	0.00023	0.00024	0.00005	0.00050
120	0.28702	0.00025	0.00001	0.00011	0.00034	0.00034
240	0.28693	0.00012	0.00003	0.00002	0.00019	0.00019
480	0.28693	0.00007	0.00003	0.00004	0.00003	0.00007

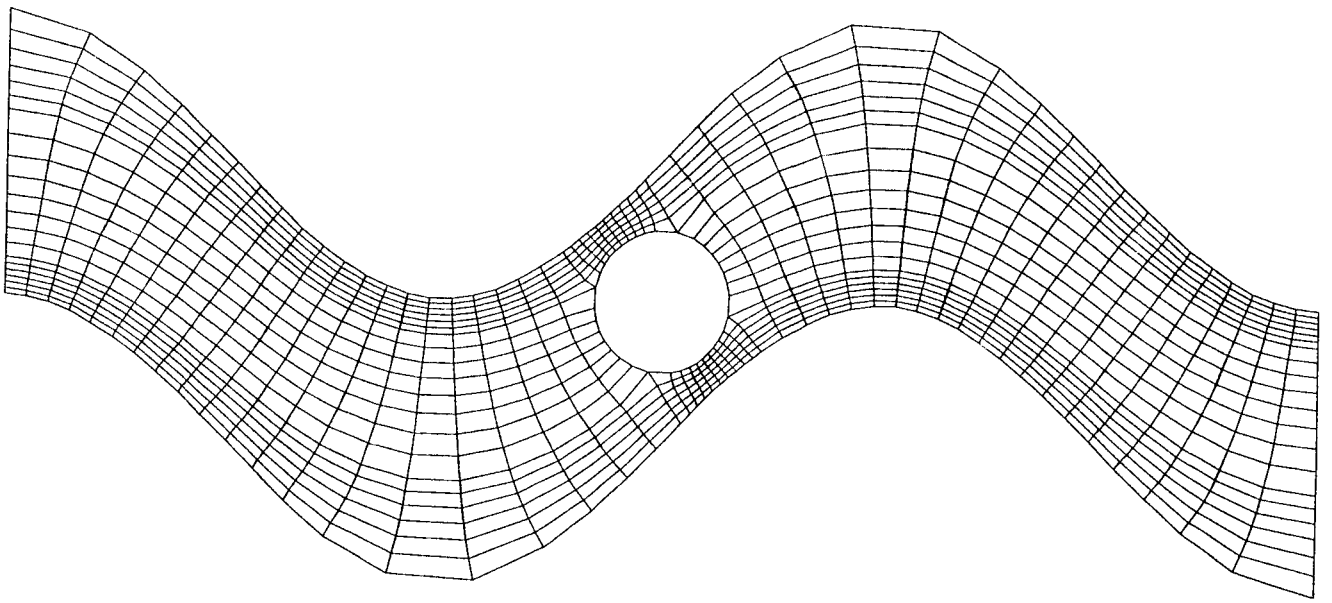

Figure 10 | Example of conformal mesh for a meandering channel and an island.

Figure 9b. Since the geometry in Q is symmetric in both the x and y directions, the geometry in Ω should also be symmetric in both u and v directions. Therefore the values of d_1, d_2, d_3 and d_4 in Figure 9b should also be equal. Table 4 lists four numerical test results deploying different numbers of boundary elements. As can be seen, the maximum difference between d_1, d_2, d_3 and d_4 decreases as the number of boundary elements increases, which means the domain in w-plane became more symmetrical. Figure 9c shows the conformal mesh generated for this doubly-connected region, with 480 boundary elements for the forward mapping, and 101×101 regular grids for the backward mapping. Figure 10 shows a mesh generated for a more general geometry where an island is located in the middle of a meandering channel.

5. CONCLUSIONS

A novel method of numerical conformal mapping is presented in this paper. The method is based on the Cauchy-Riemann conditions for the analytic function. By this method, a general polygonal region with curved

edges is directly mapped onto a regular polygon with the same number of edges, and a multiply-connected region is mapped onto a regular region with the same connectivity. Thus the computational region is similar to the original physical region in the sense that the edges on the z-plane are one to one correspondent to that in the w-plane. This will be very useful when applied to hydrodynamic and environmental modelling, since it will make the boundary condition specification much easier than the methods that map z-plane onto an up-half plane. Several numerical examples are given, for both simply connected and multiply-connected regions.

REFERENCES

Brebbia, C. A. & Dominguez, J. 1989 *Boundary Elements, An Introductory Course*. McGraw-Hill Book Company.

Chandler-Wilde, S. N. & Lin, B. L. 1992 A finite difference method for the shallow water equations with conformal boundary-fitted mesh generation. In *Hydraulic and Environmental Modelling: Coastal Waters* (ed. R. A. Falconer, S. N. Chandler-Wilde & S. Q. Liu), pp. 507–518. Ashgate Publishing.

Chaudhry, M. A. & Schinzinger, 1992*a* Numerical computation of the Schwarz-Christoffel transformation parameters for conformal mapping of arbitrarily shaped polygons with finite vertices. *Int. Jl Computation Math. electric. electron. Engng* **II**(1), 263–275.

Chaudhry, M. A. & Schinzinger, 1992*b* An extended Schwarz-Christoffel transformation for numerical mapping of polygons with curved segments. *Int. Jl Computation Math. electric. electron. Engng* **II**(2), 277–293.

Elcrat, A. R. & Trefethen, L. N. 1986 Classical free-streamline flow over a polygonal obstacle. *J. computation. appl. Math*. **14**, 251–265.

Henrici, P. 1986 *Applied and Computational Complex Analysis*, vol. III. Wiley, New York.

Gill, P.E., Murray, W. & Wright, M. H. 1991 *Numerical Linear Algebra And Optimisation*, volume 1. Addison-Wesley.

Kirby, T. K., Dalrymple R. A. & Kaku, H. 1994 Parabolic approximations for water waves in conformal co-ordinate systems. *Coastal Engng* **23**, 185–213.

Kress, R. 1989 Linear integral equations. *Applied Mathematical Sciences*, vol. 82, Springer-Verlag.

Lin, B. & Chandler-Wilde, S. N. 1996 A depth-integrated 2-D coastal and estuarine model with conformal boundary-fitted mesh generation. *Intl Jl numer. Methods Fluids* **23**, 819–846.

Papamichael, N. 1989 Numerical conformal mapping onto a rectangle with applications to the solution of Laplacian problems. *J. computat. appl. Math*. **28**, 63–83.